

Laboratory and numerical study on an enhanced evaporation process in a loess soil column subjected to heating^{*}

Xiao-chuan LIU, Wen-jie XU^{†‡}, Liang-tong ZHAN, Yun-min CHEN

(MOE Key Laboratory of Soft Soils and Geoenvironmental Engineering, Zhejiang University, Hangzhou 310058, China)

[†]E-mail: wenjiexu@zju.edu.cn

Received May 15, 2016; Revision accepted June 22, 2016; Crosschecked June 26, 2016

Abstract: The water vapor diffusion can be enhanced by the heating from municipal solid waste, and significantly impact the evaporation process in the earthen final cover. The parameters associated with the water vapor diffusion are usually measured by using the instantaneous profile method. This method is very time-consuming because the drying process lasts a long time. In this study, a bottom heating method is proposed to accelerate the drying process in a loess soil column. A constant temperature of 70 °C is applied at the bottom of the soil column. The thermo-hydraulic response of the loess is monitored along the soil column. A numerical model is developed to simulate the coupled thermo-hydraulic process. The numerical model is used to back analyze the tortuosity τ of the loess for vapor diffusion and the parameter a of an empirical evaporation function. We found that the bottom heating accelerated the drying process of the soil column by almost 22 d compared with the conditions without heating under the same evaporation boundary. Before Day 15, the proportions of the enhanced vapor flux in the total water loss were higher than 50%, dominating the evaporation process. The experimental and numerical study demonstrated that the proposed heating method is able to obtain the parameters of vapor diffusion more efficiently than the conventional method.

Key words: Soil column, Heating, Evaporation, Water vapor diffusion, Thermo-hydraulic coupled model
<http://dx.doi.org/10.1631/jzus.A1600246>

CLC number: TU411.93

1 Introduction

Previous research and field studies indicated that compacted clay covers were prone to cracking due to frost damage and desiccation (Corser *et al.*, 1992; Benson and Othman, 1993; Othman *et al.*, 1994; Leung and Chan, 2009). Composite covers were very effective at minimizing percolation. However, the associated cost was high (Shackelford, 2005). The failures occurring on the geomembrane interfaces seriously impacted the stability of the composite covers. All the above issues have led to

increased interests in earthen final covers (EFCs) in drier regions. The working principle of EFCs is like a sponge. They store water in rainy days, and release water by evaporation and plant transpiration primarily in sunny days. Deep percolation takes place only if the water storage is greater than the storage capacity. The Alternative Cover Assessment Project (ACAP) organized in the USA involved 15 EFCs (Bolen *et al.*, 2001; Albright and Glendon, 2002). Most of the monitored data and field evidences demonstrated that EFCs performed well at limiting deep percolation in arid and semi-arid areas.

In the northwest of China, loess is widely distributed, and the local climate is mainly arid and semi-arid. The use of loess as EFCs material is promising. As shown in Fig. 1, a full-scale loess final cover testing facility was constructed at the Xi'an Landfill of municipal solid waste (MSW) (Zhan,

[‡] Corresponding author

* Project supported by the National Basic Research Program (973 Program) of China (No. 2012CB719800), and the National Natural Science Foundation of China (Nos. 51378466 and 51508504)

ORCID: Xiao-chuan LIU, <http://orcid.org/0000-0002-9917-5075>
© Zhejiang University and Springer-Verlag Berlin Heidelberg 2016

2015). It was well instrumented for long-term monitoring for the performance of the loess final cover. The surface energy and water balances, based on water, water vapor, and heat transport in soils, are critical for the performance evaluation of EFCs in arid or semi-arid regions (Scanlon *et al.*, 2005). As shown in Fig. 2, the water balance of the loess final cover is mainly affected by two processes: infiltration and evapotranspiration. The MSW below the loess final cover usually has a higher temperature due to bio-degradation. Dach and Jager (1995) stated that the maximum MSW temperatures of 60 to 70 °C and up to 85 °C were measured in anaerobic and aerobic zones, respectively. Under this temperature gradient, not only water flow, but also the enhanced water vapor diffusion impacts the evaporation process of the loess final cover and cannot be ignored. The accuracy of parameters associated with vapor diffusion is essential to the modeling of the evaporation process of the loess final cover. Compared with the parameters for the wetting process, the parameters for the drying process are seldom measured because of the long time involved. In the evaporation of the stress-controllable soil column test performed by Ng and Leung (2012), it required about 105 to 210 d at the vertical net normal stresses of 4, 39, and 78 kPa to measure the drying permeability functions of water. Song *et al.* (2014) reported that water loss at the soil surface was quicker than that in deeper zones. The evaporation rate was strongly dependent on the air conditions. The traditional methods to speed up the evaporation process are applying the heating from solar or infrared radiation or a continuous wind across the soil surface (Meerdink *et al.*, 1996; Tristáncho *et al.*, 2012). These methods can only accelerate the drying process of the near-surface zone, whereas these have not much effect on the deeper zones.

The conventional methods for measuring the parameters or properties for the drying process are quite time-consuming. The effect of water vapor diffusion enhanced by heating from MSW on the evaporation process of EFCs has also not been studied systematically. This paper aims to develop a new bottom heating method to accelerate the drying process of soil and obtain the parameters associated with vapor diffusion and evaporation boundary. A soil column testing apparatus was developed in the laboratory.

A constant temperature of 70 °C was applied at the bottom of the soil column to supply the heating. The top of the column was kept open to the atmosphere to permit evaporation. The responses of the soil column, such as temperature, suction, and water content, were monitored. A numerical model was proposed to simulate the coupled thermo-hydraulic process. The tortuosity τ of the loess for vapor diffusion and the parameter a of an empirical evaporation function were obtained by back analysis using the proposed numerical model.



Fig. 1 Full-scale testing facility at the Xi'an Landfill

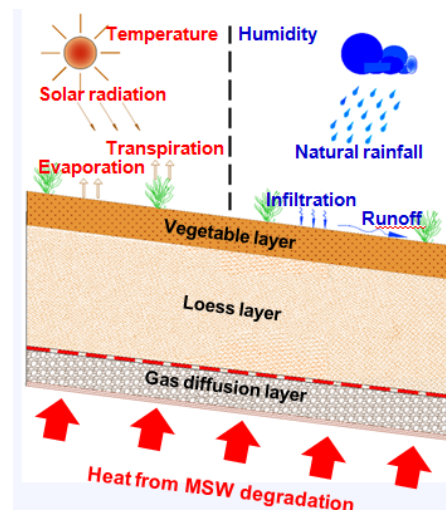


Fig. 2 Structure and boundary conditions of the loess final cover

2 Testing apparatus and instrumentation

2.1 Testing apparatus

The soil column testing apparatus consisted of a 0.8 m high acrylic hollow cylinder, a Mariotte bottle, and a heating system. As shown in Fig. 3, the hollow cylinder housed in four same sections was 200 mm in

inner diameter and 15 mm in thickness. Each section was 200 mm long. A constant water head could be applied on the top of the column by using a Mariotte bottle (Fig. 4). It was achieved by adjusting the elevation of the tube tail in the Mariotte bottle to the same level as that of the ponding head on the top of the column. The heating system consisted of a thermostatic controller and a perforated, stainless-steel plate at the bottom of the column. The thermostatic controller could keep the plate at a constant temperature (Fig. 3).

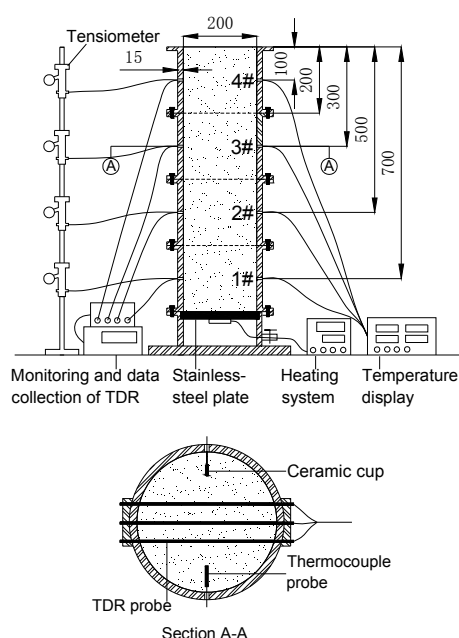


Fig. 3 Soil column testing apparatus during the heating stage (unit: mm)

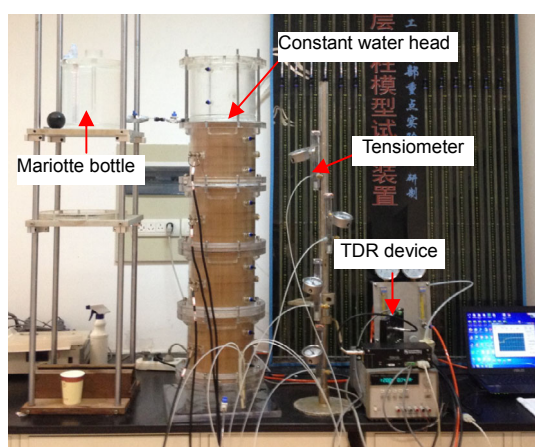


Fig. 4 Soil column testing apparatus during the infiltration stage

2.2 Instrumentation

As shown in Fig. 3, a tensiometer, a time-domain reflectometry (TDR) probe, and a thermocouple probe were installed at the middle height of each section along the soil column. Tensiometers (Soilmoisture Equipment Co., 2005) were used to measure soil suctions in the range of 0 to approximately 85 kPa. Prior to installation, each tensiometer was fully saturated with deaired water, and its response time was checked to ensure that it was free of plugging. TDR probes were used to measure the gravimetric water content. As the section of A–A in Fig. 3 shows, the three-rod TDR probe was fixed on both sides of the column. This arrangement aimed to measure the mean water content of the whole cross section of the column and had no effect on the signal of the TDR (Nissen *et al.*, 2003). The fundamental working principle of the TDR probe was the one-step TDR method (Yu and Drnevich, 2004). Laboratory calibration was conducted before the test (ASTM, 2005) to obtain the calibration constants (i.e., a , b , c , d , f , and g). The measurement accuracy of the TDR probe used in this study was $\pm 2\%$ for gravimetric water content. Considering the influence zone of the TDR probe, the distance between the ceramic cup of the tensiometer and TDR probe was set greater than 40 mm (Fig. 3). Thermocouples were used to measure the temperature. The four thermocouples were connected to a temperature display (Fig. 3). The accuracy of the used thermocouples was $\pm 1^\circ\text{C}$. The temperature and relative humidity of the laboratory were also measured by a humidity-temperature compound sensor. The accuracy of the relative humidity and temperature measurement were $\pm 2\%$ and $\pm 1^\circ\text{C}$, respectively.

To restrict water-leakage from the drilled holes for the probes, the holes were all covered by a plastic tube ending with rubber O-rings. The validation test had been performed and the results indicated that the waterproof for the probe holes was functional.

3 Test material, sample preparation, and testing procedure

The tested soil was the loess taken from an excavated slope near the Xi'an Landfill. The soil had a natural gravimetric water content of 16.5% and a dry

density of 1.508 g/cm^3 . The other physical indices of the loess are presented in Table 1. The loess could be classified as silty clay.

Table 1 Physical properties of the tested loess

Index property	Value
Percentage of particles ($>0.075 \text{ mm}$) (%)	2.20
Silt content ($0.005\text{--}0.075 \text{ m}$) (%)	71.80
Clay content ($<0.005 \text{ mm}$) (%)	26
Specific gravity	2.71
Maximum dry density (g/cm^3)	1.705
Optimum gravimetric water content (%)	19.30
Plastic limit (%)	22
Liquid limit (%)	36.70
Plasticity index	14.7
Saturated permeability ($\rho_d=1.45 \text{ g/cm}^3$) (m/s)	1.95×10^{-7}

Fig. 5 shows the laboratory measurement of the drying and wetting soil water characteristic curves (SWCCs) for the compacted loess with a dry density of 1.45 g/cm^3 . The SWCCs were best fitted using the van Genuchten equation. According to the fitting curves, the air-entry value was about 13.4 kPa and the saturated water content θ_s was about 48%. A significant hysteresis existed between the drying and wetting curves. The water content near the zero suction on the wetting curve was about 10% lower than that on the drying curve.

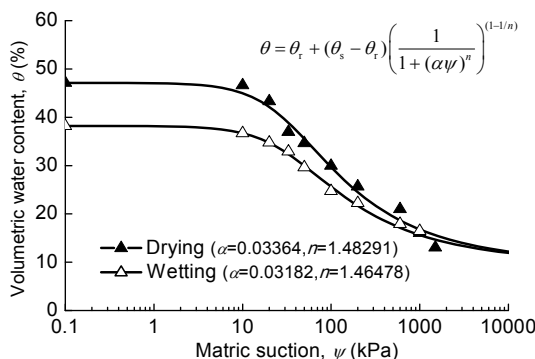


Fig. 5 Drying and wetting SWCCs of the compacted loess with a dry density of 1.45 g/cm^3

The natural loess samples were first broken up with a rubber hammer and filtered through a 2 mm aperture sieve. Then the samples were further oven-dried and mixed with water to achieve a controlled gravimetric water content of 13.2%. Before

placement of the samples within the column, a thin film of vacuum grease was placed on the inside wall of the column. This was intended to help minimize side-wall leakage during infiltration and friction during compaction. The samples were then dynamically compacted in 32 layers of 25 mm each in the column. The dry density of each layer was controlled to 1.45 g/cm^3 . Once the samples were compacted to the middle height of each section, a three-rod TDR probe, a thermocouple probe, and a metal rod of 6 mm diameter were set on the surface of the compacted layer. During the infiltration, the metal rods would be removed to install the tensiometers. This arrangement was adopted because the ceramic cup of the tensiometer was fragile.

The test consisted of two stages: infiltration and heating. The infiltration stage started when a 5 cm constant water head was applied on the top of the soil column. The soil column was wetted gradually from top to bottom. The bottom of the column was kept opened during the infiltration. After about 3 d , water began to drip out from the bottom. The outflow was collected in a storage tank and measured by recording changes of the water weight. When the rate of outflow remained constant, the infiltration stage was considered to be completed.

After infiltration, the constant water head was removed and the top of the column was kept open to the atmosphere. The bottom of the column was simultaneously sealed and subjected to a constant temperature of 70°C . During the heating stage, variations of water content, suction, and temperature along the soil column were continuously recorded by timing. The heating stage was considered to be completed when the tensiometer at 4# (Fig. 3) recorded a suction of 80 kPa to minimize the effects of cavitation. After the power of the heating system was shut down, the measurements were recorded for another 6 d .

4 Governing equations

To simulate the aforementioned heating stage, a thermo-hydraulic coupled numerical model was established, in which heat transport and two-phase flow processes were involved. The advection and diffusion controlling vapor transfer were involved in this model. The material properties (such as the SWCCs

and relative permeabilities of both water and gas phases) for the modeling were based on the previously performed laboratory tests (Zhan, 2015). The water phase was assumed to be incompressible. The gas phase was compressible and obeyed the ideal gas law. The water vapor in the gas phase was considered. The vapor diffusion is described by Fick's law. The primary variables in this model were temperature T , suction p^c , and gas pressure p^g . The soil column was assumed as a continuum homogenous porous medium.

The mass balance equations for water and gas are expressed as follows (Sanavia *et al.*, 2005; Wang *et al.*, 2009; Xu *et al.*, 2014):

$$\begin{aligned} n\left(\rho^w - \rho^{gw}\right)\left(\frac{\partial S_w}{\partial p^c} \frac{\partial p^c}{\partial t}\right) + (1 - S_w)n\left(\frac{\partial \rho^{gw}}{\partial p^c} \frac{\partial p^c}{\partial t}\right) \\ - \operatorname{div}\left(\rho^g \frac{M_a M_w}{M_g^2} \mathbf{D} \operatorname{grad}\left(\frac{p^{gw}}{p^c}\right)\right) \\ + \operatorname{div}\left(\rho^w \frac{k k^{rw}}{\mu^w} \left[-\operatorname{grad}(p^g) + \operatorname{grad}(p^c) + \rho^w \mathbf{g}\right]\right) \quad (1) \\ + \operatorname{div}\left(\rho^{gw} \frac{k k^{rg}}{\mu^g} \left[-\operatorname{grad}(p^g) + \rho^g \mathbf{g}\right]\right) = 0, \\ -n\rho^{ga}\left(\frac{\partial S_w}{\partial T} \frac{\partial T}{\partial t} + \frac{\partial S_w}{\partial p^c} \frac{\partial p^c}{\partial t}\right) \\ + (1 - S_w)n\left(\frac{\partial \rho^{ga}}{\partial T} \frac{\partial T}{\partial t} + \frac{\partial \rho^{ga}}{\partial p^c} \frac{\partial p^c}{\partial t} + \frac{\partial \rho^{ga}}{\partial p^g} \frac{\partial p^g}{\partial t}\right) \quad (2) \\ - \operatorname{div}\left(\rho^g \frac{M_a M_w}{M_g^2} \mathbf{D} \operatorname{grad}\left(\frac{p^{ga}}{p^c}\right)\right) \\ + \operatorname{div}\left(\rho^{ga} \frac{k k^{rg}}{\mu^g} \left[-\operatorname{grad}(p^g) + \rho^g \mathbf{g}\right]\right) = 0, \end{aligned}$$

where n is the porosity, S_w is the water saturation, \mathbf{k} is the material intrinsic permeability tensor, k^{rw} and k^{rg} are the relative permeabilities of the water phase and gas phase, and M_a , M_w , and M_g are the molar masses of the dry air phase, water phase, and gas phase, respectively. Gas phase was mixed from the vapor and dry air. p^{gw} and p^{ga} are the partial pressures of water vapor and dry air, respectively, and \mathbf{g} is the gravity acceleration. ρ^w , ρ^{gw} , ρ^g , ρ^{ga} are the densities of the water, water vapor, gas phase, and dry air, respectively. \mathbf{D} is the effective diffusivity tensor, and varies with the saturation, temperature, and gas

pressure, which can be described as

$$D = n(1 - S_w)\tau D_0 \left(\frac{T}{T_0}\right)^{1.8} \frac{p_0}{p^g}, \quad (3)$$

where τ is the tortuosity which is an essential parameter for modeling of the vapor diffusion and would be obtained by numerical modeling and back analysis in the following paragraphs, and $D_0=2.58\times10^{-5}$ m²/s is the diffusion coefficient of the vapor in the air at the reference temperature $T_0=273.15$ K and pressure $p_0=101325$ Pa. The density of the water vapor can be calculated by an empirical function (Rutqvist *et al.*, 2001):

$$\rho^{gw} = 10^{-3} e^{19.891 - 4975/T} e^{-p^c M_w / (\rho^w R T)}. \quad (4)$$

The gas phase is assumed to be a mixture of dry air and water vapor. According to the equation of the state of perfect gas and Dalton's law, the water vapor pressure p^{gw} can be written as

$$p^{gw} = \rho^{gw} RT / M_w. \quad (5)$$

The van Genuchten function is applied in this study to describe the relationship between the suction and water saturation, which can be written as (van Genuchten, 1980)

$$p^c = p_0 (S_e^{m/(1-m)} - 1)^{1/m}, \quad (6)$$

$$S_e = \frac{S_w - S_{wr}}{1 - S_{wr} - S_{gr}}, \quad (7)$$

where p_0 is the gas entry pressure, m is a shape factor for van Genuchten model, S_e is the effective saturation, and S_{wr} and S_{gr} are the residual water and gas saturation, respectively.

The water and gas flow are described by the extended Darcy's law for unsaturated porous medium. The relative permeabilities for both water and gas phases are considered and have the following form (Wang *et al.*, 2011):

$$k^{rw} = S_e^{1/2} \left[1 - \left(1 - S_e^{m/(m-1)}\right)^{(m-1)/m} \right]^2, \quad (8)$$

$$k^{rg} = (1 - S_e)^{1/2} (1 - S_e^{m/(m-1)})^{2(1-1/m)}. \quad (9)$$

The energy balance equation of the unsaturated medium is (Kolditz *et al.*, 2012a):

$$\begin{aligned} C^w \rho^w \frac{kk^{rw}}{\mu^w} [-\text{grad}(p^g) + \text{grad}(p^c) + \rho^w \mathbf{g}] \text{grad}(T) \\ + C^g \rho^g \frac{kk^{rg}}{\mu^g} [-\text{grad}(p^g) + \rho^g \mathbf{g}] \text{grad}(T) \\ + C \rho \frac{\partial T}{\partial t} - \text{div}(\lambda \text{grad}(T)) = q_{th}, \end{aligned} \quad (10)$$

where $C\rho = nS_w C^w \rho^w + n(1-S_w)C^g \rho^g + (1-n)C^s \rho^s$ is the heat capacity of the porous medium, where C^w , C^g , and C^s are the specific heat capacities of water, gas, and solid, respectively. $\lambda = nS_w \lambda^w + n(1-S_w)\lambda^g + (1-n)\lambda^s$ is the heat conductivity of the porous medium. λ^w , λ^g , and λ^s are the heat conductivities of water, gas, and solid, respectively.

This numerical model has been implemented into the finite element method (FEM) numerical code OpenGeoSys (OGS) (Kolditz *et al.*, 2012b). The method of weighted residuals is applied to derive the weak formulation of the balance equations for a two-phase flow and heat transport. The Galerkin method is used to discretize the weak forms of the balance equations. The generalized Trapezoidal method finite differences in time are used to solve the initial value problem (Lewis and Schrefler, 1998).

5 Numerical model

An axial symmetric FEM model is set up. The mesh discretization and model dimension are shown in Fig. 6. The initial condition of the gas pressure is assumed to equal the atmospheric pressure, and the suction distribution in the soil column is applied according to the measurement of tensiometers. The initial temperature of the soil column is 19.2 °C. The bottom boundary is assumed to be impervious for both gas and water phases, and the temperature is fixed at 70 °C during the heating stage and would be deactivated after that. The lateral boundary of the model is also assumed to be impervious for the water and gas phases, and defined as a heat transport boundary because the soil column is exposed in the

laboratory without any insulation measure. The heat transport is proportional to the temperature differences between the soil column and the laboratory air. The top boundary is pervious for the water and gas phases and the gas pressure is assumed to be constant as the atmospheric pressure. A specific evaporation boundary is applied. Based on Song (2014), the rate of evaporation can be calculated with an empirical function which has the following form:

$$E_a = E_p \frac{H_s - H_r}{1 - H_r} = (a + b \cdot n_{wind})(100 - H_r) \frac{H_s - H_r}{1 - H_r}, \quad (11)$$

where E_a is the evaporation rate, E_p is the evaporation potential, H_r is the relative humidity of the air, H_s is the relative humidity of the surface soil, and n_{wind} is the wind speed, which is neglected in this study (the indoor wind speed is approximately equal to zero). a and b are empirical parameters of the empirical function. b is considered as zero. a would be obtained by numerical modeling and back analysis in the following paragraphs. Material parameters for the numerical modelling are listed in Table 2.

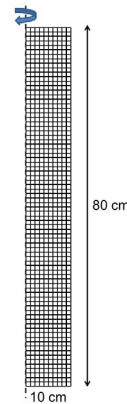


Fig. 6 The mesh discretization and model dimension of FEM model

6 Results and analysis

Fig. 7 shows the temperature contour on Day 5 after the heating was started. The numerical results indicate that the heating bottom has a greater impact on the increase of the temperature only in the lower part of the soil column. The temperature has a slight decrease from the axis to the lateral boundary. This is because the lateral boundary was defined as a heat

transport boundary. The generated heat escaped into the out air in the laboratory through it. Although the heat flow was not 1D, the lateral boundary was impervious for the water and gas phases and the water flow and water vapor diffusion were both 1D. The key point of this paper is the enhanced water vapor diffusion during the evaporation process subjected to heating.

Table 2 Material parameters for numerical modeling

Parameter	Value
Porosity, n	0.465
Intrinsic permeability, k (m^2)	1.45×10^{-14}
Parameter of van Genuchten model, p_0 (Pa)	31400
Parameter of van Genuchten model, m	0.32
Heat conductivity of soil, λ^s ($\text{W}/(\text{m}\cdot\text{K})$)	0.26
Heat conductivity of water, λ^w ($\text{W}/(\text{m}\cdot\text{K})$)	0.60
Heat conductivity of gas, λ^g ($\text{W}/(\text{m}\cdot\text{K})$)	0.026
Specific heat capacity of soil, C^s ($\text{J}/(\text{kg}\cdot\text{K})$)	1600
Specific heat capacity of water, C^w ($\text{J}/(\text{kg}\cdot\text{K})$)	4200
Specific heat capacity of gas, C^g ($\text{J}/(\text{kg}\cdot\text{K})$)	1010



Fig. 7 Temperature contour on Day 5 after the heating was started (unit: °C)

The tortuosity τ of the tested loess was obtained by repeatedly adjusting the value of itself until the simulated response of the loess had a best agreement with the measured results. Finally, the value of τ was defined as 0.65. Fig. 8 presents the measured and simulated temperature distributions with time.

Days 0 and 37 indicate the start and end of the heating, respectively. The average initial measured temperature of the soil column was 19.2 °C. The temperature measured at 1# drastically increased to about 40 °C on Day 1 and kept at such a value until the heating was stopped. The temperature measured at

the other three depths (i.e., 2#, 3#, and 4#) increased only by 2.5–5.5 °C on Day 1 and then changed between 20 and 27 °C during the heating stage. It can be found that the variation of temperature was not significant at the upper part of the soil column, which indicates that the effect of heating is limited.

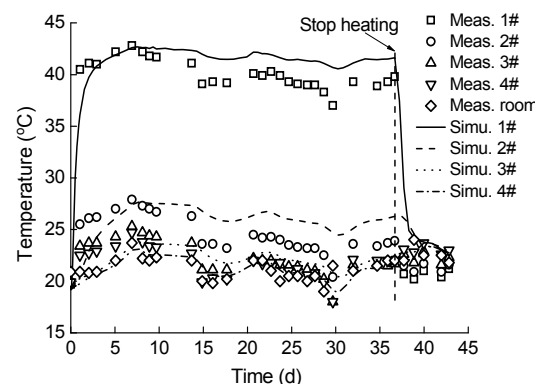


Fig. 8 Measured and simulated temperature distributions with time

As there was not any insulation measure for the soil column, the temperature inside the soil column was sensitive to that in the laboratory. The developments of temperature show a similar trend between each other. The trend of simulated results has a good agreement with that of the measured ones, and the discrepancies in magnitude are small or moderate. The reason for such discrepancies may be that of the errors in the estimates for the thermal properties such as specific heat capacity or thermal conductivity of the compacted loess.

Fig. 9 depicts a comparison between the measured and simulated suction distributions with time. It can be seen that the measured suctions all continuously increased. The measured suction at 4# had a greater increase rate than the other three ones. It is because the tensiometer at 4# is closer to the evaporation boundary (i.e., the surface of soil column). After the heating was stopped, the measured suctions all kept increasing but with a lower rate. The solid points mean that the cavitation had occurred in the tensiometer at 4#, and the value could not represent the real suction in the loess. The general trends between measured and simulated results agree well, with some moderate differences in magnitude. For example, the simulation underestimates the measured suction at 4# and 2# (the maximum error is about 10 kPa).

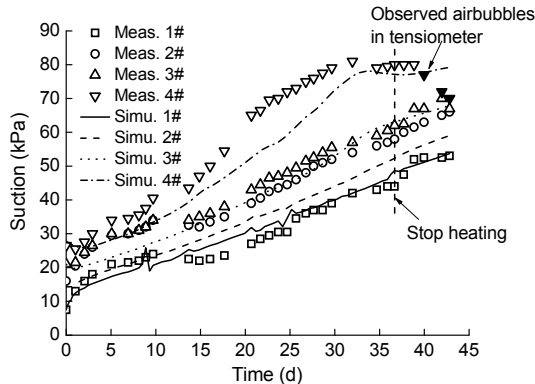


Fig. 9 Measured and simulated suction distributions with time

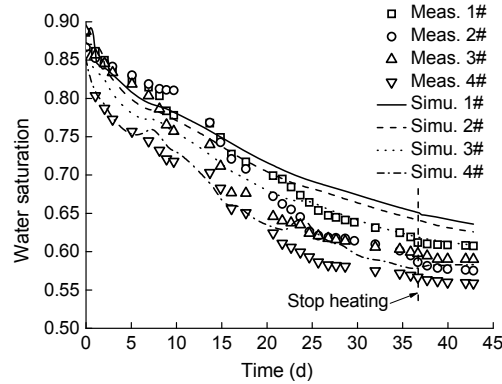


Fig. 10 Measured and simulated water saturation distributions with time

Fig. 10 describes the measured and simulated water saturation distributions with time. It is noted that the measured saturation was calculated from the water content measured by TDR probes. The simulated saturation was derived from the simulated suction in Fig. 9 using Eqs. (6) and (7). The measured settlement deformation of the whole soil column after the infiltration stage was about 1 mm. It may be due to the high compaction degree (85%) of the loess. In fact, the deformation in this magnitude has not much effect on the initial dry density (i.e., 1.45 g/cm³) of the whole soil column. Thus, the dry density was considered as the initial value during the heating stage and in the numerical modeling.

The measured saturations at four depths all decreased gradually at the same time from the initial value of 80%–90% to 55%–65%. The measured saturations at 4# and 1# both have a significant decrease after the heating was started. The middle part of the soil column (i.e., 2# and 3#) has a later and slower decrease of saturation at the beginning of heating. After the heating was stopped, the measured saturations all still kept decreasing but with a lower rate, which is in accord with the results of the suction distribution in Fig. 9. In general, the measurements of the experiment are well represented by the numerical results. After Day 20, the simulation overestimates the measured saturation. The differences may be due to the error in the estimate for the water contents measured by the TDR probes. The measurement accuracy of the TDR probes used in this study was $\pm 2\%$ which could result in an error of about $\pm 5\%$ in saturation.

The parameter a of the empirical evaporation function was obtained by the same method used in the acquirement of tortuosity τ until the simulated evaporation rates had a best agreement with the measured ones. Finally, the value of a was determinated as 0.022 mm/d. The evaporation rate and relative humidity distributions with time are shown in Fig. 11. The measured evaporation rates were calculated by the integral of volumetric water content profiles for the depth of the soil column at different time points. The simulated evaporation rate was calculated by Eq. (11). As shown in Fig. 11, during the heating stage, the change of relative humidity in the laboratory is significant from 21% to 72.5%. An obvious negative relationship between the measured relative humidity and evaporation rate can be observed. The relative humidity refers to an ability of air at a certain temperature for accommodating water vapor. When the relative humidity in the laboratory increases approaching 100% (i.e., the saturation condition), it means there is little space in the air for accommodating any more water vapor. As a result, the evaporation rate decreases, and vice versa.

Fig. 11 shows that the general trend of the measured evaporation rate decreased progressively over time. Because the total amount of water in the soil column gradually reduced (Fig. 10), there was less and less water which could be evaporated. The general trend of measured results could be well represented by the simulated ones. It is noted that the applied evaporation empirical function (Eq. (11)) was appropriate for modeling this condition in the laboratory test.

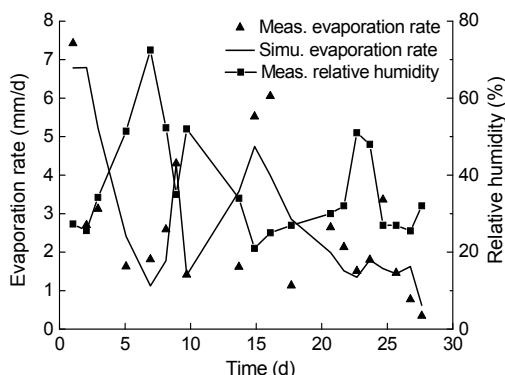


Fig. 11 Evaporation rate and relative humidity distributions with time

Fig. 12 presents the measured suction profiles along the soil column at different time points. It can be found that the measured suctions in the upper part were always higher than those in the lower part during and after heating. The generated suction gradient impelled the water to transport from the lower part (i.e., hot end) to the upper part (i.e., cold end), which is just contrary to the direction of water transport in the sealed soil column. Fig. 13 shows the simulated gas pressure profiles along the soil column at different time points. Just like the measured suction profiles shown in Fig. 12, the simulated gas pressures in the upper part were always lower than those in the lower part during and after heating. The generated gas pressure gradient impelled water vapor to transport from the lower part to the upper part. The directions of the water and water vapor transport were both from the bottom to the top of the soil column in this test.

To further understand the acceleration of the drying processes by bottom heating, the evaporation of the soil column without heating was also simulated. The model, boundary conditions, and parameters were all the same as those used in the simulation with heating. The comparisons of water saturations with and without heating are shown in Fig. 14. The obvious quantitative discrepancies can be observed between the two results. The decrease rates of measured water saturations were all significantly greater than those of the simulated ones. As Fig. 14 shows, the measured water saturations at 3# and 4# with heating were spent about 22 d earlier in arriving at the same value than the numerical ones without heating under the same evaporation boundary, while

they were 20 d earlier at 1# and 2#. In other words, the bottom heating could accelerate the drying process of the soil column by almost 22 d, because the water was “extracted out” from the column mainly through water flow from the bottom to the top of the column without heating. When subjected to a heating at the bottom, the water in the lower part of the column evaporated, which generated a significant gas pressure gradient. The water vapor diffusion was subsequently enhanced. As shown in Figs. 12 and 13, the directions of the water flow and water vapor diffusion were both from the bottom to the top. Both the water flow and water vapor diffusion contributed to the drying process of the soil column. For the loess final covers in the field, the acceleration of the drying processes induced by the heating from MSW could help to release the stored water in it and improve its performance.

Actually, water vapor diffusion also exists during the evaporation without heating although its amount is small. The bottom heating significantly

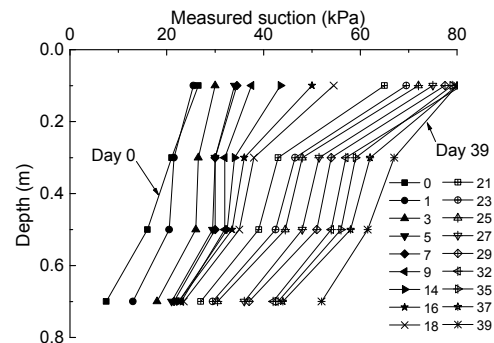


Fig. 12 Measured suction profiles along the soil column at different time points

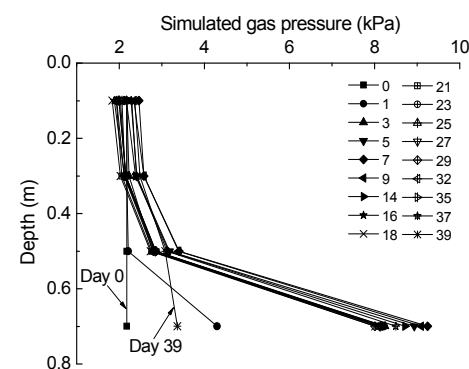


Fig. 13 Simulated gas pressure profiles along the soil column at different time points

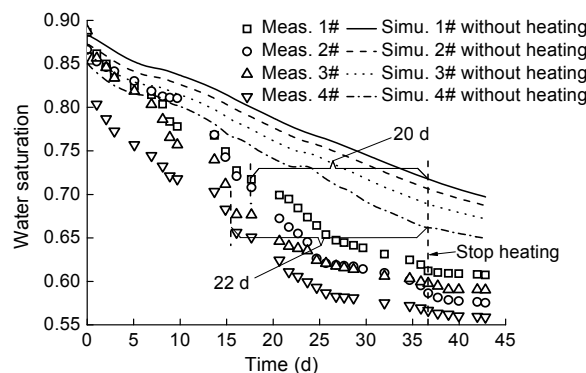


Fig. 14 Comparison of water saturations with and without heating

enhanced water vapor diffusion and it cannot be ignored any more. To quantitatively investigate the contribution of enhanced water vapor diffusion to the total water loss with heating, it can be assumed as the difference between the measured water saturation decrease with heating and the simulated one without heating. Thus, the proportion of enhanced vapor flux in the total water loss by heating could be defined as:

$$\begin{aligned} W_{\text{Heating}}^t &= \frac{(S_w^0 - S_{w, \text{heating}}^t) - (S_w^0 - S_{w, \text{non-heating}}^t)}{S_w^0 - S_{w, \text{heating}}^t} \\ &= \frac{S_{w, \text{non-heating}}^t - S_{w, \text{heating}}^t}{S_w^0 - S_{w, \text{heating}}^t}, \end{aligned} \quad (12)$$

where S_w^0 is the initial water saturation, and $S_{w, \text{heating}}^t$ and $S_{w, \text{non-heating}}^t$ are the water saturations at time t with and without heating, respectively. The results are shown in Fig. 15. The proportions of enhanced vapor flux increased significantly to almost 76% on Day 1. Then the proportions instantly decreased. From Day 3 to the end, the proportions continuously decreased but with a lower rate. It can be found that before Day 15 the proportions of enhanced vapor flux at 1#, 2#, and 3# were always higher than 50%. After Day 15, the proportions decreased from 50% to 25%. Day 15 was a watershed (the watershed was Day 19 for the proportions at 4#). Before that, water vapor diffusion dominated the evaporation process, while after that water flow did. The vapor flux depends on the water vapor pressure p^{gw} , while the water vapor pressure p^{gw} depends on the density of the water vapor ρ^{gw} (Eq. (5)). Eq. (4) shows that the magnitude of water

vapor density ρ^{gw} depends on the value of temperature T and suction p^c . When suction p^c stays unchanged, the density of water vapor ρ^{gw} increases with an increase of temperature T . When temperature T is a constant, the density of the water vapor ρ^{gw} decreases with an increase of suction p^c . Thus, at the beginning of the heating (i.e., Day 1), the suction p^c was relatively small. The abrupt increase of temperature T resulted in a significant increase of the water vapor density ρ^{gw} , as well as the water vapor pressure p^{gw} and vapor flux. Then the temperature T at four depths kept relatively steady (Fig. 8), but the suction p^c all continuously increased (Fig. 9). As a result, the density of the water vapor ρ^{gw} , as well as the water vapor pressure p^{gw} and vapor flux, accordingly decreased.

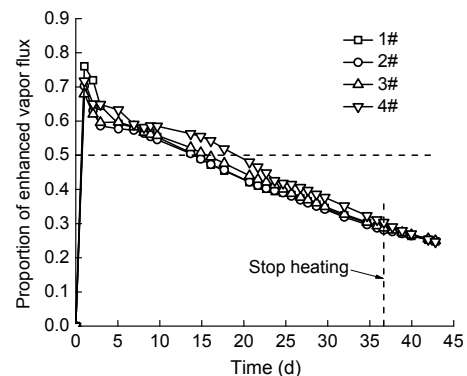


Fig. 15 Proportion of enhanced vapor flux in total water loss by heating with time

7 Conclusions and future work

A laboratory loess soil column test subjected to a constant high temperature at the bottom was performed. The response of the soil column was monitored and a numerical model was proposed to simulate the coupled thermo-hydraulic process. The main conclusions are as follows:

1. The tortuosity τ of the tested loess for vapor diffusion and the parameter a of the empirical evaporation function were obtained by back analysis using the proposed numerical model. Finally, the tortuosity τ and parameter a were defined as 0.65 and 0.022 mm/d, respectively.

2. The heating of the bottom accelerated the drying process of the soil column by almost 22 d compared with the conditions without heating, which

indicated that the proposed new method is time-saving. The water vapor diffusion was significantly enhanced by the bottom heating.

3. Before Day 15 the proportions of enhanced vapor flux in the total water loss with heating were always higher than 50%, which indicated that water vapor diffusion dominated the evaporation process at this period. After Day 15, the proportions decreased from 50% to 25%.

Futher studies should focus on the modeling of the long-term performance of the loess final cover in the field using the obtained parameters and proposed coupled model presented in this paper.

References

- Albright, W.H., Glendon, W.G., 2002. Alternative Cover Assessment Project (ACAP): Phase I Report. Desert Research Institute, USA.
- ASTM (American Society for Testing and Materials), 2005. Standard Test Method for Water Content and Density of Soil in Place by Time Domain Reflectometry (TDR), D6780-05. National Standards of the USA.
- Benson, C., Othman, M., 1993. Hydraulic conductivity of compacted clay frozen and thawed *in situ*. *Journal of Geotechnical Engineering*, **119**(2):276-294.
[http://dx.doi.org/10.1061/\(ASCE\)0733-9410\(1993\)119:2\(276\)](http://dx.doi.org/10.1061/(ASCE)0733-9410(1993)119:2(276))
- Bolen, M.M., Roesler, A.C., Benson, C.H., et al., 2001. Alternative Cover Assessment Program: Phase II Report. Geo-Engineering Report.
- Corser, P., Pellicer, J., Cranston, M., 1992. Observations on the Long Term Performance of Composite Clay Liners and Covers. Geotechnical Fabrics Report, p.6-16.
- Dach, J., Jager, J., 1995. Prediction of gas and temperature with the disposal of pretreated residential waste. Proceedings of the 5th International Waste Management and Landfill Symposium, CISA, Italy, I:665-677.
- Kolditz, O., Görke, U., Shao, H.B., et al., 2012a. Thermo-Hydro-Mechanical-Chemical Processes in Porous Media. Springer, Berlin Heidelberg, Germany, p.89.
<http://dx.doi.org/10.1007/978-3-642-27177-9>
- Kolditz, O., Bauer, S., Bilke, L., et al., 2012b. OpenGeoSys: an open-source initiative for numerical simulation of thermo-hydro-mechanical/chemical (THM/C) processes in porous media. *Environmental Earth Sciences*, **67**(2): 589-599.
<http://dx.doi.org/10.1007/s12665-012-1546-x>
- Leung, M.K.H., Chan, K.Y., 2009. Theoretical and experimental studies of heat transfer with moving phase-change interface in freezing and thawing of porous potting soil. *Journal of Zhejiang University-SCIENCE A*, **10**(1):1-6.
<http://dx.doi.org/10.1631/jzus.A0820263>
- Lewis, R.W., Schrefler, B.A., 1998. The Finite Element Method in the Static and Dynamic Deformation and Consolidation of Porous Media, 2nd Edition. Wiley, New York, USA, p.508.
- Meerdink, J.S., Benson, C.H., Khire, M.V., 1996. Unsaturated hydraulic conductivity of two compacted barrier soils. *Journal of Geotechnical Engineering*, **122**(7):565-576.
[http://dx.doi.org/10.1061/\(ASCE\)0733-9410\(1996\)122:7\(565\)](http://dx.doi.org/10.1061/(ASCE)0733-9410(1996)122:7(565))
- Ng, C.W.W., Leung, A.K., 2012. Measurements of drying and wetting permeability functions using a new stress-controllable soil column. *Journal of Geotechnical and Geoenvironmental Engineering*, **138**(1):58-68.
[http://dx.doi.org/10.1061/\(ASCE\)GT.1943-5606.0000560](http://dx.doi.org/10.1061/(ASCE)GT.1943-5606.0000560)
- Nissen, H.H., Ferré, T., Moldrup, P., 2003. Sample area of two- and three-rod time domain reflectometry probes. *Water Resources Research*, **39**(10), No. 1289.
<http://dx.doi.org/10.1029/2002WR001303>
- Othman, M., Benson, C., Chamberlain, E., Zimmie, T., 1994. Laboratory testing to evaluate changes in hydraulic conductivity caused by freeze-thaw: state-of-the-art. *Hydraulic Conductivity and Waste Containment Transport in Soils*, STP1142, ASTM, p.227-254.
<http://dx.doi.org/10.1520/STP23890S>
- Rutqvist, J., Böggesson, L., Chijimatsu, M., et al., 2001. Thermohydromechanics of partially saturated geological media: governing equations and formulation of four finite element models. *International Journal of Rock Mechanics and Mining Sciences*, **38**(1):105-127.
[http://dx.doi.org/10.1016/S1365-1609\(00\)00068-X](http://dx.doi.org/10.1016/S1365-1609(00)00068-X)
- Sanavia, L., Pesavento, F., Schrefler, B.A., 2005. Finite element analysis of non-isothermal multiphase geomaterials with application to strain localization simulation. *Computational Mechanics*, **37**(4):331-348.
<http://dx.doi.org/10.1007/s00466-005-0673-6>
- Scanlon, B.R., Reedy, R.C., Keese, K.E., et al., 2005. Evaluation of evapotranspirative covers for waste containment in arid and semiarid regions in the southwestern USA. *Vadose Zone Journal*, **4**(1):55-71.
<http://dx.doi.org/10.2136/vzj2005.0055>
- Shackelford, C.D., 2005. Environmental issues in geotechnical engineering. Proceedings of the 16th International Conference on Soil Mechanics and Geotechnical Engineering, Osaka, Japan. ICSMGE, Millpress, Rotterdam, The Netherlands, **16**(1):95-122.
- Song, W.K., 2014. Experimental Investigation of Water Evaporation from Sand and Clay Using an Environmental Chamber. PhD Thesis, Université Paris-Est, Paris, France.
- Song, W.K., Cui, Y.J., Tang, A.M., et al., 2014. Experimental study on water evaporation from sand using environmental chamber. *Canadian Geotechnical Journal*, **51**(2): 115-128.
<http://dx.doi.org/10.1139/cgj-2013-0155>
- Soilmoisture Equipment Co., 2005. Operation Instructions: The Model 2100F Soilmoisture Probe. Goleta, CA, USA.

- Tristano, J., Caicedo, B., Thorel, L., et al., 2012. Climatic chamber with centrifuge to simulate different weather conditions. *Geotechnical Testing Journal*, **35**(1):159-171.
<http://dx.doi.org/0.1520/GTJ103620>
- van Genuchten, M.T., 1980. A closed-form equation for predicting the hydraulic conductivity of unsaturated soils. *Soil Science Society of America Journal*, **44**(5):892-898.
<http://dx.doi.org/10.2136/sssaj1980.03615995004400050002x>
- Wang, W., Kosakowski, G., Kolditz, O., 2009. A parallel finite element scheme for thermo-hydro-mechanical (THM) coupled problems in porous media. *Computers & Geosciences*, **35**(8):1631-1641.
<http://dx.doi.org/10.1016/j.cageo.2008.07.007>
- Wang, W., Rutqvist, J., Gorke, U.J., et al., 2011. Non-isothermal flow in low permeable porous media: a comparison of unsaturated and two-phase flow approaches. *Environmental Earth Sciences*, **62**(6):1197-1207.
<http://dx.doi.org/10.1007/s12665-010-0608-1>
- Xu, W.J., Shao, H., Hesser, J., et al., 2014. Numerical modelling of moisture controlled laboratory swelling/shrinkage experiments on argillaceous rocks. In: Norris, S., Bruno, J., Cathelineau, M. (Eds.), *Clays in Natural and Engineered Barriers for Radioactive Waste Confinement*. Geological Society of London, London, p.359-366.
<http://dx.doi.org/10.1144/SP400.29>
- Yu, X., Drnevich, V.P., 2004. Soil water content and dry density by time domain reflectometry. *Journal of Geotechnical and Geoenvironmental Engineering*, **130**(9):922-934.
[http://dx.doi.org/10.1061/\(ASCE\)1090-0241\(2004\)130:9\(922\)](http://dx.doi.org/10.1061/(ASCE)1090-0241(2004)130:9(922))
- Zhan, T.L., 2015. Moisture and gas flow properties of compacted loess final covers for MSW landfills in Northwest China. The 6th Asian-Pacific Region Conference of Unsaturated Soil Mechanics, Guilin, China.

中文摘要

题 目：黄土土柱加热加速蒸发的试验模拟研究

目 的：土质覆盖层下的城市固体废弃物由于生化降解反应具有更高温度，该温度梯度增强了土质覆盖层内的水蒸气扩散，在覆盖层的蒸发模拟中不容忽视。与水蒸气扩散相关的参数一般通过瞬态剖面法测量，但在一定蒸发边界下的土体干燥过程会持续很长时间，因此这种传统测量方法十分耗时。本文旨在提出一个底部加热的新方法加速黄土土柱脱湿，更为高效地获取水蒸气运移相关参数。

创新点：1. 提出一个全新的底部加热方法用于加速土体脱湿，同时利用提出的数值模型反分析得到水蒸气运移的相关参数挠曲度 τ ; 2. 发现底部加热加速脱湿的根本原因在于极大增强的水蒸气扩散。

方 法：1. 研制一套室内黄土土柱试验装置（图3）；2. 在土柱底部施加恒温 70 °C，监测黄土的水热响应（图4）；3. 提出一个数值模型模拟这一水热耦合运移过程，利用该模型反分析影响水蒸气运移的关键参数，包括试验黄土的挠曲度 τ 和经验蒸发公式的参数 a 。

结 论：1. 在相同蒸发边界下，相比不加热的情况，底部加热使土柱脱湿加速了最高 22 天；2. 在第 15 天前，加热增强的水蒸气流量主导黄土蒸发过程，一直占总水分损失量的 50% 以上；3. 试验及数值模拟结果均表明，相比传统方法，本文提出的底部加热法可更为高效地获取水蒸气运移参数。

关键词：土柱；加热；蒸发；水蒸气扩散；水热耦合模型